Chemical Science

ROYAL SOCIETY OF CHEMISTRY

EDGE ARTICLE

View Article Online
View Journal | View Issue

Cite this: *Chem. Sci.*, 2023, **14**, 12264

All publication charges for this article have been paid for by the Royal Society of Chemistry

Variation from closed-shell to open shell electronic structures in oligothiophene bis(dioxolene) complexes†

Paul D. Miller,[a] David A. Shultz, *[a] Joshua Mengell, [b] Martin L. Kirk *[bcd] and Lukasz Wojtas[e]

A series of oligothiophene bis(dioxolene) complexes, **SQ–Th$_n$–SQ** (SQ = $S = \frac{1}{2}$Tp^{Cum,Me}Zn^{II}(3-*tert*-butyl-orthosemiquinonate); Tp^{Cum,Me} = tris(5-cumenyl-3-methylpyrazolyl)borate anion) have been synthesized, structurally characterized, and studied as a function of the number of thiophene bridging units, n (n = 0–3) using a combination of variable–temperature (VT) electronic absorption and EPR spectroscopies, and VT magnetic susceptibility measurements. The thiophene bridge bond lengths determined by X-ray crystallography display dramatic differences across the **SQ–Th$_n$–SQ** series. Bridge bond deviation values ($\Sigma|\Delta_i|$) display a progressive change in the nature of the bridge fragment bonding as the number of thiophene groups increases, with quinoidal bridge character for n = 1 (**SQ–Th–SQ**) and biradical character with "aromatic" bridge bond lengths for n = 3 (**SQ–Th$_3$–SQ**). Remarkably, for n = 2 (**SQ–Th$_2$–SQ**) the nature of the bridge fragment is intermediate between quinoid and biradical aromatic, which we describe as having open-shell character as opposed to biradicaloid since the open-shell biradical configuration does not have the correct symmetry to mix with the quinoidal ground-state configuration. This bridge bonding character is reflected in the energies of the lowest lying open-shell states for these three molecules. The **SQ–Th–SQ** molecule is diamagnetic at all temperatures studied, and we provide evidence for **SQ–SQ** antiferromagnetic exchange coupling and population of triplet states in **SQ–Th$_2$–SQ** and **SQ–Th$_3$–SQ**, with J_{SQ-SQ}(ave) = −279 cm^{-1} (VT EPR/electronic absorption/magnetic susceptibility) and J_{SQ-SQ} = −117 cm^{-1} (VT EPR/electronic absorption/magnetic susceptibility), respectively. The results have been interpreted in the context of state configurational mixing within a simplified 4-electron, 3-orbital model that explicitly contains contributions of a bridge fragment. Variable–temperature spectroscopic- and magnetic susceptibility data are consistent with two low-lying open-shell states for **SQ–Th$_3$–SQ**, but three low-lying states (one closed-shell and two open-shell) for **SQ–Th$_2$–SQ**. This model provides a simple symmetry-based framework to understand the continuum of electronic and geometric structures of this class of molecules as a function of the number of thiophene units in the bridge.

Received 5th May 2023
Accepted 7th October 2023

DOI: 10.1039/d3sc02341a

rsc.li/chemical-science

Introduction

Conjugated π-systems that possess biradical character[1–6] hold tremendous promise as novel architectures for molecular and molecule-based materials due to their remarkable magnetic, optical, and electronic properties. As a result, these π-conjugated biradical systems are expected to contribute to the organic semiconductor,[7–9] singlet fission,[1] break junction,[10] spintronics,[11,12] non-linear optical, and exchange-coupled electron spin qubit[13–17] knowledge base and function as models for understanding the effects of dipolar coupling and molecular vibrations on spin relaxation.[18] It has recently been shown that the introduction of biradicaloid character into the bridge fragment in break-junction molecular conductance studies dramatically modifies the distance dependence of the conductance,[10,19,20] leading to reversed conductance decay behavior

[a]*Department of Chemistry, North Carolina State University, Raleigh, North Carolina 27695-8204, USA. E-mail: shultz@ncsu.edu*

[b]*Department of Chemistry and Chemical Biology, The University of New Mexico, MSC03 2060, 1 University of New Mexico, Albuquerque, NM 87131-0001, USA. E-mail: mkirk@unm.edu*

[c]*The Center for High Technology Materials, The University of New Mexico, Albuquerque, New Mexico 87106, USA*

[d]*Center for Quantum Information and Control (CQuIC), The University of New Mexico, Albuquerque, New Mexico 87131-0001, USA*

[e]*Department of Chemistry, University of South Florida, 4202 E. Fowler Avenue, CHE 205, Tampa, FL 33620-5250, USA*

† Electronic supplementary information (ESI) available: Experimental details. Synthetic-, X-ray crystallographic-, and magnetic susceptibility details and data. CCDC 2260981–2260983. For ESI and crystallographic data in CIF or other electronic format see DOI: https://doi.org/10.1039/d3sc02341a

where an increase in conductance with increasing molecular wire length is observed.[10,20] One-dimensional molecular wires typically display an exponential distance dependence on conductance in the coherent tunneling regime.[21–24] This biradicaloid conductance study[20] is important since, in the context of the Su, Schrieffer and Heeger model,[25,26] biradical species have 1-D topological insulator properties. Namely, they possess occupied and unoccupied delocalized states and localized topologically protected conducting edge states in the bandgap region.

Along with Chichibabin's hydrocarbon derivatives and analogs,[1,27–30] phenoxy radicals are the most common organic radical employed in the construction of conjugated π-systems with biradicaloid character, and their magnetic, optical, and vibrational properties have been extensively studied (Fig. 1A).[1,3,4,31–36] These compounds display small HOMO–LUMO gaps, and the large spin density on the *para*-carbon of 3,6-di-*tert*-butylphenoxy[37] when bonded to thiophene bridge units results in strong through-bond coupled, closed-shell ground states that are NMR-active for bridges comprised of 0–4 thiophene units,[38–40] although characteristics of open-shell configurations have been reported for **Phen–Th$_2$–Phen**.[32,34] In contrast to oligothiophene-bridged structures, a single *para*-phenyl bridge unit results in a closed-shell quinoidal electronic structure,[36] but two-[41,42] or more *para*-phenylene bridge units result in thermally-accessible open-shell character. Understanding biradical electronic structure has been complicated due to various experimental issues and the challenging nature of the open-shell computational problem. Here, we present the results of a detailed structural, magnetic, and spectroscopic study on a series of **SQ–Th$_n$–SQ** (n = 0–3) molecules in order to gain greater insight into the electronic structure of these biradical systems, and discuss the results of these studies in terms of the quinoid, biradical, and biradicaloid character in the electronic ground and excited states of these molecules.

Biradicaloid systems have consistently been described in terms of two Lewis structures that are in resonance (Fig. 1). These resonance structures are the closed-shell quinoid form and open-shell biradical from, the latter of which derives from a HOMO → LUMO one-electron promotion. This idea leads to the possibility of a continuum of biradicaloid descriptions, with the biradical and quinoid forms at the extrema and "biradicaloid" describing a quantum mechanical admixture (*i.e.*, resonance) of open-shell biradical and quinoid. Additional complexity exists in such systems where the open-shell biradical Lewis structure can distort (*e.g.*, along a torsional coordinate), which leads to non-planar structures. Here, the electronic structures of the low-lying biradical and quinoid states have been described as being in thermal equilibrium with one another, although experimental evidence for this equilibrium has been limited.[29]

The first biradicaloid was synthesized in 1907 (Chichibabin's hydrocarbon; **CH**, Fig. 1B)[43] and inspired decades of controversy that was described as the "Biradical Paradox".[44,45] The paradox being: solution EPR of **CH** indicated $|J| \ll |a|$ (a = isotropic proton hyperfine coupling constant), despite clear evidence that $|J|$ was in fact much larger than $|a|$ due to the diamagnetic character displayed by the compound. Many studies were conducted to explain this phenomenon,[44–49] however it wasn't until 1987 that Montgomery, *et al.*[50] conclusively showed through X-ray diffraction that **CH** contained a quinoidal bond length pattern. Upon obtaining a pure sample of **CH**, it was actually found to be EPR silent due to the magnitude of $|J|$, and paramagnetic impurities (dimers,[51] or radical quenching through proton abstraction[52]) were responsible for the conflicting results. However, it is important to note that there are still non-covalent interactions between radicals that can complicate the

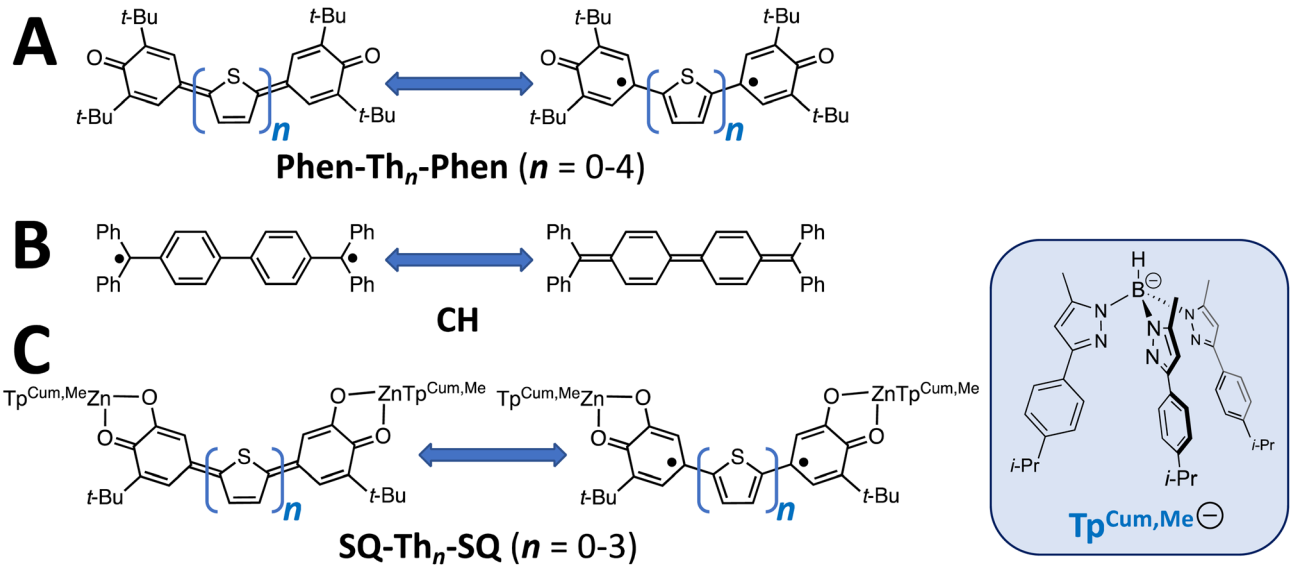

Fig. 1 (A) Kekulé π-systems comprised of phenoxy radical-terminated oligothiophenes. (B) Chichibabin's hydrocarbon, **CH**. (C) Bis(semiquinone) complexes presented in this study.

analysis, and obfuscate the electronic structure description of biradicaloids.[45]

Metal complexes of $S = \frac{1}{2}$ orthosemiquinone (SQ) are powerful alternatives to phenoxy radical-based molecules since they allow for the inclusion of both diamagnetic and paramagnetic transition metal ions into the molecular scaffold. In addition, the spin density distribution of SQ *vs.* phenoxy places ~65% less spin density for SQ at the point of attachment[37] to a bridging organic π-system (positions marked with "●" in Fig. 1A and C). Thus, the incorporation of SQ allows for thermal population of the triplet state at lower temperatures compared to phenoxy biradicals. Herein, we present dinuclear metal complexes comprised of two bridge terminal SQ groups, where both SQs are complexed to a diamagnetic $(Tp^{Cum,Me}Zn^{II})^+$ complex ion ($Tp^{Cum,Me}$ = tris(5-cumenyl-3-methylpyrazolyl) borate[53–55] bridged by 0–3 thiophene groups; Fig. 1C). The $Tp^{Cum,Me}$ anionic ligand was first used for steric protection of SQ groups by Pierpont,[55] and subsequently by us.[21,56–61] Our crystallographic results clearly show a decrease in "quinoidal" bond lengths as the number of thiophene bridge fragments increases. This observation is consistent with both variable–temperature magnetic susceptibility results as well as variable–temperature electronic absorption spectroscopic studies, which illustrate thermal population of the exchange coupled triplet state with increasing temperature. In addition, we present molecular orbital (MO) and state models that provide a fundamental symmetry-based framework to understand the continuum of electronic structures in this class of molecules as a function of the number of thiophene units in the bridge.

Results and analysis

Here, we present synthetic results, X-ray crystallographic results, and associated analyses for the **SQ–SQ**, **SQ–Th–SQ**, **SQ–Th$_2$–SQ**, and **SQ–Th$_3$–SQ** series of compounds. Since their ground state electronic structures span a continuum from closed-shell singlet quinoidal to open-shell singlet biradical, we will present analyses of the magnetic and spectroscopic results together for each compound at the end of this section. Detailed computations and electronic absorption band assignments for **SQ–Th–SQ** and **SQ–Th$_2$–SQ** and **SQ–Th$_3$–SQ** are beyond the scope of this manuscript and will be presented elsewhere.

Synthesis and structural data

Synthetic details and structural data are presented in the ESI† and below for all complexes in this study.

Synthesis of SQ–Th$_n$–SQ molecules. A series of oligothiophene bis(semiquinone) complexes (**SQ–SQ**, **SQ–Th–SQ**, **SQ–Th$_2$–SQ**, and **SQ–Th$_3$–SQ**) were synthesized as illustrated in Scheme S1 (see ESI†). Suzuki coupling of the oligothiophene (n = 1–3) dibromide with $MOM_2CatBpin$ yielded the respective $(MOM_2Cat)_2Th_n$ (n = 1–3). Methoxymethyl (MOM) deprotections are performed by subjecting $(MOM_2Cat)_2Th_n$ (n = 1–3) to concentrated HCl in CH_2Cl_2/MeOH and stirring overnight. Scheme S2† illustrates the differing synthetic pathway toward **SQ–SQ**. Suzuki coupling of $MOM_2CatBpin$ to MOM_2CatBr yields $(MOM_2Cat)_2$, which is then subjected to the same sequence of reactions as the **SQ–Th$_n$–SQ** series. Complexing Cat_2Th_n (n = 0–3) with $Tp^{Cum,Me}Zn(OH)$ in the presence of K_2CO_3 in CH_2Cl_2/MeOH was then performed under an inert atmosphere. Subsequently, the reactions were then opened to air and stirred overnight to allow for CAT oxidation to SQ to yield the final complexes.

X-ray crystallographic structure determination and analysis. X-ray quality crystals were grown for **SQ–SQ** and **SQ–(Th)$_n$–SQ** (n = 1–3) and their structures were obtained *via* X-ray diffraction (Fig. 2, 3 and Table S4†). The average ring torsion angles for the dioxolene groups relative to each other (**SQ–SQ**) or relative to the bridge (**SQ–Th$_n$–SQ**) are 0.64° (**SQ–SQ**), 3.93° (**SQ–Th–SQ**), 10.16° (**SQ–Th$_2$–SQ**), and 14.76° (**SQ–Th$_3$–SQ**). We also calculate bond deviation parameters, $\Sigma|\Delta_i|$, from the absolute value of the difference between the bond lengths of the dioxolene moieties for each compound and those of 3,5-di-*tert*-butyl-1,2-semiquinonate (Table S4†), which can be considered a "non-

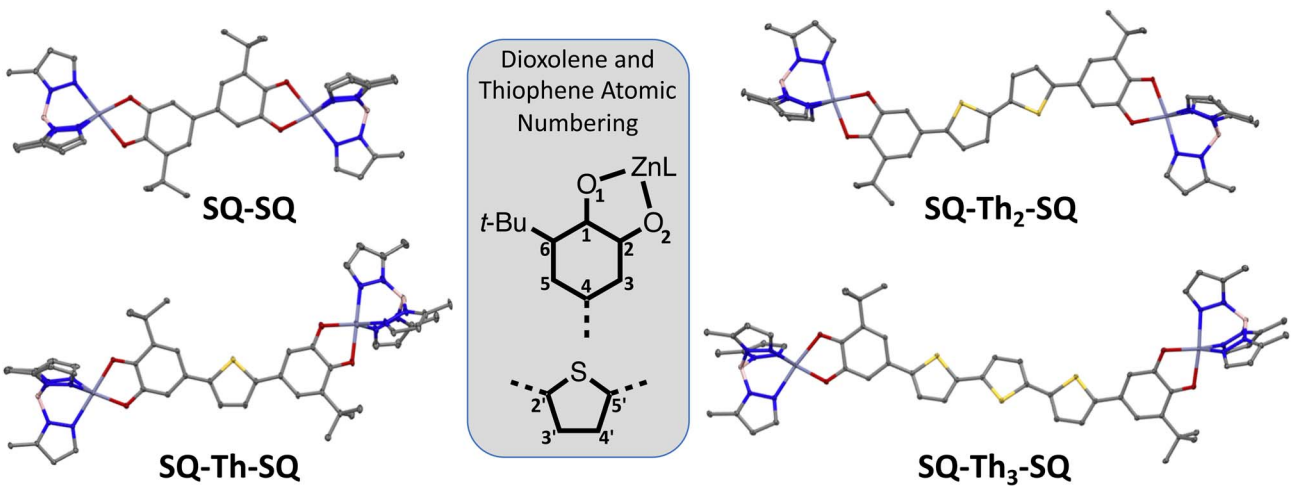

Fig. 2 Thermal ellipsoid (50% probability) plots from 100 K crystal structures of SQ_2Th, SQ_2Th_2, and SQ_2Th_3. Hydrogens and cumenyl groups are omitted for clarity.

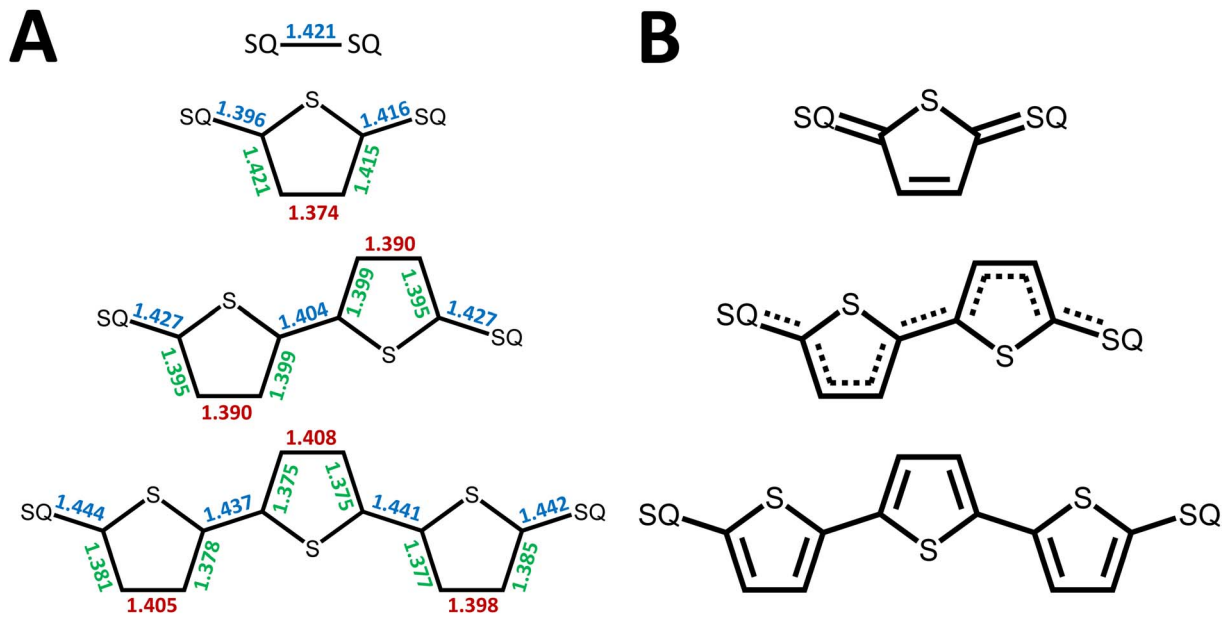

Fig. 3 (A) Relevant bridge bond lengths (in Å) from X-ray crystal structures (data collected at 100 K). Arrows denote increase in SQ-bridge bond lengths with increasing number of Th units (blue), increase in Th ring bond lengths with decreasing number of Th units (green), and increase in Th bond lengths with increasing number of Th units (red). (B) Bridge bond line drawings that correspond to the bond lengths shown in (A).

delocalized into a bridge fragment" semiquinone radical.[62] Bond deviation parameters highlight bond length changes that signify delocalization of the SQ π-system into the bridge, and the values of $\Sigma|\Delta_i|$ for **SQ–Th–SQ**, **SQ–Th$_2$–SQ**, and **SQ–Th$_3$–SQ** are 0.150 ± 0.019 Å, 0.119 ± 0.014 Å, and 0.080 ± 0.017 Å, respectively. Bond length deviation parameters were also determined for thiophene bridges by comparing the bridges of **SQ$_2$Th**, **SQ$_2$Th$_2$**, and **SQ$_2$Th$_3$** to their respective diamagnetic, fully aromatic analogs 2,5-diphenyl-thiophene,[63] 5,5′-diphenyl-2,2′-bithiophene,[64] and 3′,4′-dibutyl-5,5″-diphenyl-2,2′:5′,2″-terthiophene, respectively.[65] Only bonds between atoms within the oligothiophene π-system, excluding substituents, were included in the calculation of $\Sigma|\Delta_i|$. The bridge $\Sigma|\Delta_i|$ values were 0.110 ± 0.024 Å (**SQ–Th–SQ**), 0.081 ± 0.017 Å (**SQ–Th$_2$–SQ**), and 0.026 ± 0.028 Å (**SQ–Th$_3$–SQ**), which suggests a trend toward a more aromatic bridge unit in going from **SQ–Th$_2$–SQ** to **SQ–Th$_3$–SQ**.

Spectroscopic and magnetic data for SQ–SQ and SQ–Th–SQ

Magnetic resonance spectroscopy. Frozen glass EPR spectra were not observed for **SQ–SQ** and **SQ–Th–SQ** at 95 K in 2-MTHF. This observation is consistent with diamagnetic $S = 0$ quinoidal closed shell ground states for these complexes and no thermal population of an $S = 1$ triplet state. We also attempted to collect EPR spectra at elevated temperatures for **SQ–Th–SQ** in a poly(-vinylchloride) solid solution film matrix but we observed no signal associated with an excited triplet at temperatures as high as 360 K. Additionally, the **SQ–Th–SQ** ^{1}H-NMR spectra display no paramagnetic broadening of the aromatic proton signals (Fig. S5†), in marked contrast to **SQ–Th$_2$–SQ**, and this provides additional support that **SQ–Th–SQ** possesses a closed-shell singlet ground state with no thermally accessible triplet state(s).

Variable–temperature magnetic susceptibility measurements. Crystals grown for X-ray diffraction were used for variable–temperature (VT) magnetic susceptibility measurements. Consistent with the EPR and NMR data, the magnetic susceptibility data for **SQ–Th–SQ** also show that the ground state is diamagnetic (see ESI†) with no evidence of a paramagnetic state being thermally populated in the 5–300 K temperature range.

Electronic absorption spectroscopy. Fig. 4 displays the room temperature solution electronic absorption spectra for **SQ–SQ** and **SQ–Th–SQ** in cyclohexane. Both complexes exhibit effectively panchromatic absorption throughout the UV-visible range that, for **SQ–Th–SQ**, extends into the NIR region of the spectrum.

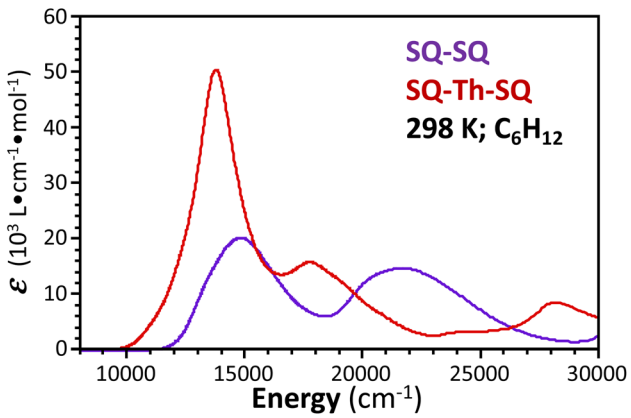

Fig. 4 Overlay of electronic absorption spectra of SQ–SQ, and SQ–Th–SQ. Spectra were recorded at room temperature as solutions in cyclohexane.

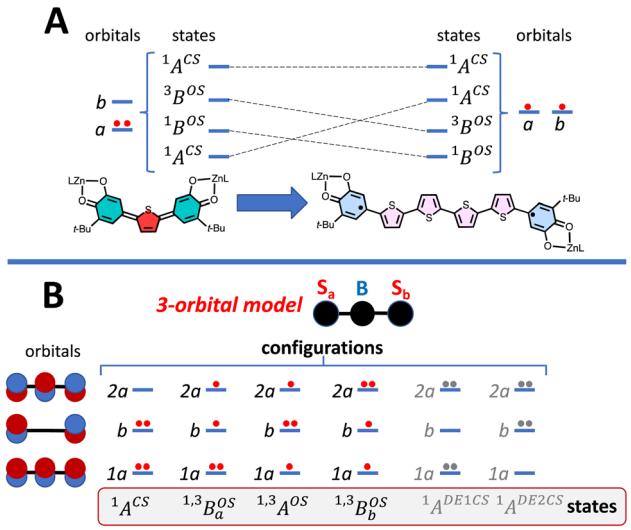

Fig. 5 Symmetrized models for understanding biradicaloid electronic structure. (A) Anderson-type 2-orbital, 4-state model. Symmetry labels A and B are generic and refer to the symmetries of molecular orbitals that are symmetric (A) and antisymmetric (B) with respect to a symmetry element that relates the two halves of the molecule. Clearly, for C_{2h} and C_{2v} structures these symmetry elements will be different, but the A and B labels remain valid. (B) 3-Orbital, 4-electron MO model (S_a = spin on left ZnSQ fragment, B = Th$_n$ bridge fragment, S_b = spin on right ZnSQ fragment) used to explain the electronic structure of the **SQ–Th$_n$–SQ** (ZnSQ$_a$-bridge-ZnSQ$_b$) complexes studied in this manuscript. Note that the superexchange interaction in this model, which leads to the $^{1,3}B_a^{OS}$ open shell singlet–triplet splitting, derives from mixing with the $^{1,3}B_b^{OS}$ excited configuration of the same symmetry. Six representative configurations and states are shown: CS = closed-shell, OS = open shell, DE1CS = lowest doubly-excited closed-shell, and DE2CS = highest doubly-excited closed-shell. The state representations are derived from the 1a, b, and 2a MO occupancies.

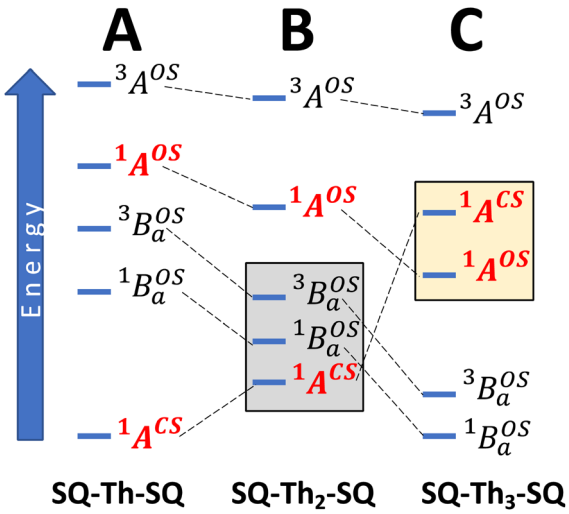

Fig. 6 State energy diagrams that derive from a 4-orbital, 3-electron model. (A) Closed-shell **SQ–Th–SQ**, (B) mixed-configuration ($^1A^{CS}$ and $^1A^{OS}$) **SQ–Th$_2$–SQ**. (C) Open-shell **SQ–Th$_3$–SQ**. Gray box in (B) highlights thermally-populated states used to fit both susceptibility and spectroscopic data for **SQ–Th$_2$–SQ**. See text for details.

Electronic structure of the SQ–SQ and SQ–Th–SQ complexes. In the active electron approximation,[58,66,67] the simplest orbital basis for describing the ground state of bis-semiquinones is constructed from the two SQ singly occupied molecular orbitals (SOMOs), labeled a and b in Fig. 5A. Thus, the orbital and state diagram in Fig. 5A details how the electronic structure of **SQ–Th$_n$–SQ** can be described in terms of an Anderson-type two orbital,[68] two electron model. This model yields 4-states,[69] and has been used for understanding biradicaloid character in similar systems.[1,6,69,70] The two-orbital model was originally developed using hydrogenic orbitals that allow for the configurational mixing of open- and closed-shell singlet configurations, since there is only one triplet configuration. Fig. 5A also shows the generalized symmetry labels for the two open-shell ($a^1b^1 \rightarrow {}^1B^{OS}$ and ${}^3B^{OS}$) and two closed-shell configurations (a^2b^0 and $a^0b^2 \rightarrow 2 \times {}^1A^{CS}$) that derive from this model in the strong coupling (non-asymptotic) limit. Importantly, when rigorous or local effective symmetry is present in these molecules, symmetry dictates that only totally symmetric $S = 0$ open-shell singlet configurations will mix with the totally symmetric $S = 0$ quinoidal configuration to generate biradicaloid character. However, within the context of this simple two-orbital model there are no open-shell singlet excited states that can mix with the quinoidal $^1A^{CS}$ ground state since the two SQ SOMOs possess different symmetries.

To account for any admixture of open-shell singlet character into the quinoidal $^1A^{CS}$ ground state the model needs to be expanded, and a minimally expanded 3-orbital, 4-electron model, with select configurations, is shown in Fig. 5B. This model includes an effective bridge orbital that provides a mechanism for excited open shell configurations to mix into the quinoidal $^1A^{CS}$ ground state. A partial state energy diagram is given in Fig. 6, which displays many features in common with Tanabe–Sugano diagrams[71,72] used to understand the nature of ligand field excitations in transition metal complexes. As one moves from **SQ–Th–SQ** to **SQ–Th$_3$–SQ**, the **SQ–SQ** interaction decreases and closed-shell configurations increase in energy, which drives the system from closed-shell quinoidal to open-shell biradical.

Crystallographically-determined bond deviation parameters and the diamagnetic nature of the complexes for **SQ–SQ** and **SQ–Th–SQ** clearly indicate that these molecules possess dominant quinoidal closed-shell $S = 0$ electronic ground states. As a result, the admixture of open shell configurations (*e.g.*, the $^1A^{OS}$ in Fig. 5) must be quite small.

Spectroscopic and magnetic data for SQ–Th$_3$–SQ

Variable–temperature magnetic susceptibility measurements. The structural data for **SQ–Th$_3$–SQ** shows a bond length pattern characteristic of aromatic Th rings (Fig. 3), and this is consistent with an open-shell ground-state electronic structure for this complex. To correlate the observed **SQ–Th$_3$–SQ** structural parameters with the ground state electronic structure, we performed variable–temperature magnetic susceptibility measurements. These data are presented as the $\chi_{para}T$ product *vs.* T in Fig. 7 and show that a paramagnetic state is populated at temperatures above ~50 K. Since the SQ moieties are more

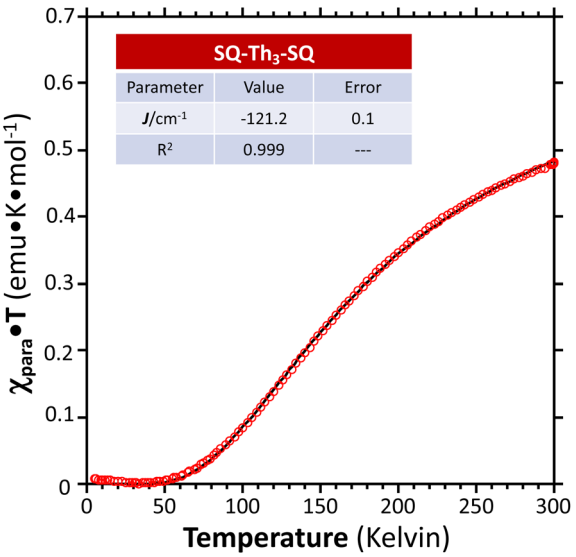

Fig. 7 Paramagnetic susceptibility-temperature product ($\chi_{para}T$) *vs.* temperature for a crystalline sample of **SQ–Th$_3$–SQ**, measured by variable–temperature magnetic susceptibility experiments at a magnetic field strength of 0.1 Tesla (data: O; fit: —).

weakly coupled than those in **SQ–SQ** and **SQ–Th–SQ**, we use an antiferromagnetically exchange coupled $S_1 = S_2 = \frac{1}{2}$ dimer model that employs the $H = -2\boldsymbol{J}(S_1 \cdot S_2)$ Heisenberg exchange Hamiltonian to generate the magnetic susceptibility expression in eqn (1), where $\boldsymbol{J}$ is the pairwise magnetic exchange coupling constant between the two SQ radical spins, k_B is the Boltzmann constant, g is the electronic g-value, and T is the temperature.

$$\chi_{para}T = 0.125\ \mathrm{g^2\ emu\ K\ mol^{-1}} \left(\frac{6e^{\left(\frac{-2J}{k_B T}\right)}}{1 + 3e^{\left(\frac{2J}{k_B T}\right)}} \right) \quad (1)$$

We fit eqn (1) to the data to yield $\boldsymbol{J} = -121\ \mathrm{cm^{-1}}$, with a corresponding singlet–triplet energy gap of $2\boldsymbol{J} = \Delta E(S - T) = 242\ \mathrm{cm^{-1}}$. The susceptibility data indicate an electronic structure that correlates with the state diagram shown in Fig. 6C, with a $^1B_a^{OS}$ ground state and an exchange coupled $^3B_a^{OS}$ triplet state at higher energy ($2\boldsymbol{J}$).

Electron paramagnetic resonance (EPR) spectroscopy. Low temperature glass and VT polymer film EPR data were collected for **SQ–Th$_3$–SQ** and are shown in Fig. 8A and B, respectively. The glass matrix data were collected at 120 K in 2-MTHF, and the spectrum in Fig. 8A is characteristic of a randomly-oriented, $S = 1$ triplet with a rhombic g-tensor.[73] Zero-field splitting (zfs) parameters, determined by simulations of the experimental spectrum, were determined to be $|\boldsymbol{D}/hc| = 0.00342\ \mathrm{cm^{-1}}$ and $|\boldsymbol{E}/hc| = 0.00062\ \mathrm{cm^{-1}}$. The exchange coupling between the two SQ radicals was determined from the temperature dependence of the EPR spectra for **SQ–Th$_3$–SQ**. In the VT experiments, **SQ–Th$_3$–SQ** was dissolved in a poly(vinyl chloride) polymer matrix and the integrated signal intensity of the $\Delta m_s = 2$ resonance at $g \sim 4$ was measured as a function of temperature. The doubly-integrated $\Delta m_s = 2$ signal is shown plotted as a function of T^{-1} in Fig. 8B. The same $\mathscr{H} = -2\boldsymbol{J}\widehat{S_1} \cdot \widehat{S_2}$ exchange Hamiltonian was used to generate eqn (2).

$$I_{EPR} \propto \chi_{para} = \frac{2\beta^2 g^2}{3k_B T} \frac{3e^{\frac{-2J}{k_B T}}}{1 + 3e^{\frac{-2J}{k_B T}}} \quad (2)$$

We fit eqn (2) to the VT EPR data to yield $\boldsymbol{J} = -119\ \mathrm{cm^{-1}}$, which is in excellent agreement with the exchange parameter determined from our analysis of the VT magnetic susceptibility data ($\boldsymbol{J} = -121\ \mathrm{cm^{-1}}$). Thus, the VT EPR data support the solid-state magnetic susceptibility data, with both data sets being consistent with an aromatic ring-bridged biradical (*i.e.*, open-shell singlet) ground state. This electronic structure determination is also fully consistent with the bond length patterns

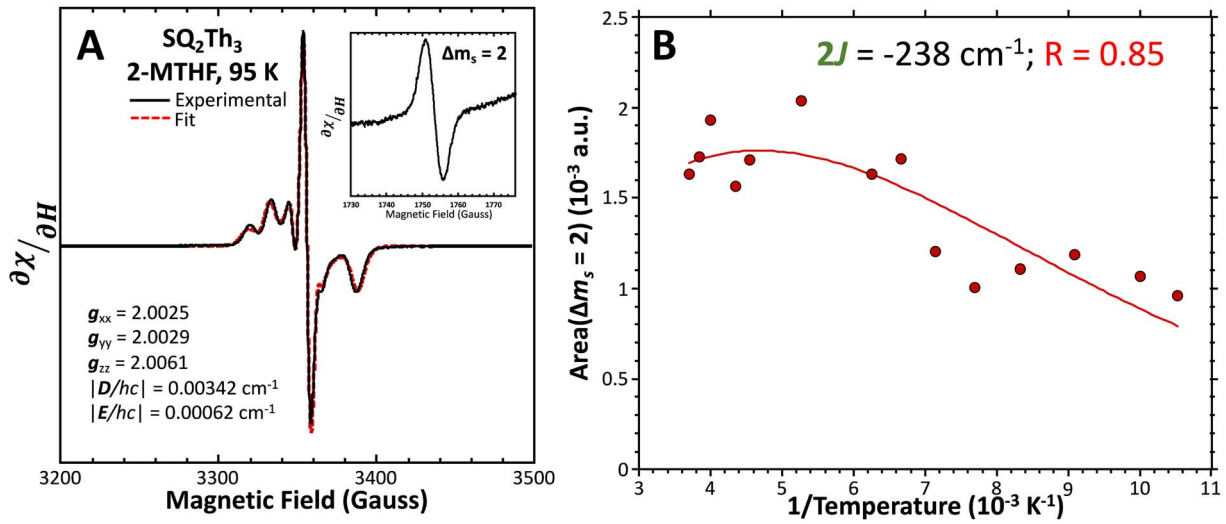

Fig. 8 (A) Powder EPR spectrum of **SQ-Th$_3$-SQ** (—) and simulation parameters. (Inset) $\Delta m_s = 2$ transition. Fit (---) includes 32% $S = \frac{1}{2}$ impurities. For simulation details, see text and ESI.† (B) Doubly-integrated $\Delta m_s = 2$ EPR transition intensities (●) *vs.* inverse temperature and fit (—) for **SQ-Th$_3$-SQ**. See text for fit details. Samples were ~1 mM dissolved in an evaporated film of poly(vinyl chloride).

($\Sigma|\Delta_i|$ values for both SQ and Th rings, *vide supra*) obtained from the X-ray structure of **SQ–Th$_3$–SQ**.

Electronic absorption spectroscopy. Complex temperature-dependent electronic absorption spectra are observed for **SQ–Th$_3$–SQ** (Fig. 9). As noted for **SQ–SQ** and **SQ–Th–SQ**, we also observe panchromatic absorption for **SQ–Th$_3$–SQ** that extends throughout the UV-visible and into the NIR region of the spectra. In marked contrast to room temperature **SQ–Th–SQ** electronic absorption data, the corresponding 296 K spectrum of **SQ–Th$_3$–SQ** exhibits structured, moderately intense bands across the entire spectral region. The VT electronic absorption spectra (Fig. 9A) were collected on a sample dissolved in a poly(styrene) thin film. Clear isosbestic points are observed at 15 540, 17 182, and 21 150 cm^{-1}, consistent with only two species contributing to the electronic absorption spectra across the 4–196 K temperature range. Since both the variable-temperature EPR and magnetic susceptibility data indicate $J \approx -120$ cm^{-1}, this leads to an $S = 0$ ground state singlet and a negligible population of the exchange coupled $S = 1$ triplet state at 4 K (at 4 K; $n_{S=1}/n_{S=0} \sim 3\exp(-242/2.78) \sim 0$). Thus, the 4 K spectrum of **SQ–Th$_3$–SQ** is that of the exchange coupled $^1B_a^{OS}$ singlet ground state.

The intensities of the temperature dependent bands at 22 422 cm^{-1} and 18 215 cm^{-1}, which we associate with the $^1B_a^{OS}$ singlet ground- and $^3B_a^{OS}$ thermally-populated triplet states, respectively, are plotted as a function of temperature in Fig. 9B. A simple 2-state (singlet and triplet) Boltzmann expression was fit to these data to yield a singlet–triplet splitting of 222 cm^{-1} ($J = -111$ cm^{-1}). This value of J determined from VT electronic absorption data is in excellent agreement with the exchange coupling parameter for **SQ–Th$_3$–SQ** that was determined from both magnetic susceptibility ($J = -121$ cm^{-1}) and variable-temperature EPR spectroscopy ($J = -119$ cm^{-1}), *vide supra*. The temperature dependent $^1B_a^{OS}$ and $^3B_a^{OS}$ contributions to the VT electronic absorption spectra of **SQ–Th$_3$–SQ** have allowed us to extract the pure individual spectra that originate from the $^1B_a^{OS}$ and $^3B_a^{OS}$ states (Fig. 10), providing additional access to the nature of the excited state manifold.

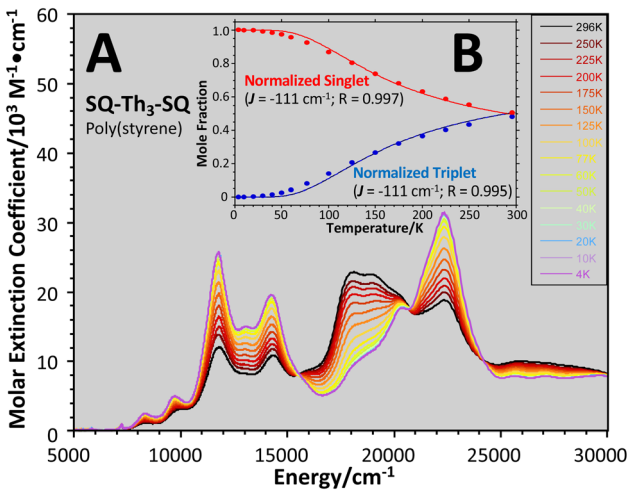

Fig. 9 (A) Variable–temperature (4–298 K) electronic absorption spectra of SQ–Th$_3$–SQ in a poly(styrene) film. (B) Normalized transition intensities (● and ●) and state populations (— and —) at 18 215 cm^{-1} (triplet) and 22 422 cm^{-1} (singlet).

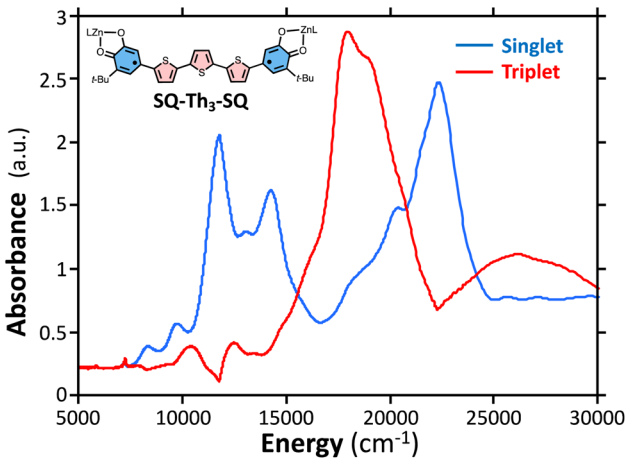

Fig. 10 Singlet spectrum of SQ–Th$_3$–SQ (—) collected at 4 K. Triplet spectrum of SQ–Th$_3$–SQ (—) derived from subtracting the weighted 4 K spectrum from the 298 K spectrum.

Considering the state description in Fig. 6C, one can have spin-allowed excitations from the open shell aromatic $^1B_a^{OS}$ ground state to configurationally mixed excited states (*e.g.*, configurationally mixed $^1A^{OS}$ and $^1A^{CS}$ in the 3-orbital model; Fig. 5B) that possess closed-shell quinoidal character. Therefore, the electronic absorption spectrum that originates from the aromatic-bridge biradical $^1B_a^{OS}$ ground state contains transitions to biradicaloid/open-shell singlet excited states. In marked contrast, there are no triplet excited states that possess closed-shell quinoidal character. This is why the spectra that originate from the $^1B_a^{OS}$ and $^3B_a^{OS}$ states are very different in their appearance, and strongly suggests considerable mixing between open- and closed-shell excited singlet configuration states. Strong mixing between these singlet excited states can drive one or more of these states below the lowest energy excited triplet state, and this is the likely origin for the dramatic red shift of the singlet spectrum compared to the triplet spectrum (Fig. 10).

Spectroscopic and magnetic data for SQ–Th$_2$–SQ

Variable–temperature magnetic susceptibility measurements. Crystals grown for X-ray diffraction were used to perform VT magnetic susceptibility measurements on **SQ–Th$_2$–SQ** and the data are shown in Fig. 11. These data confirm that the sample is diamagnetic up to ~120 K. At higher temperatures, a slight increase in $\chi_{para}T$ is observed, and this is indicative of an $S = 1$ triplet state being thermally populated.

Electron paramagnetic resonance (EPR) spectroscopy. The EPR spectrum of **SQ–Th$_2$–SQ** in a solid solution polymer film matrix is provided in Fig. 12A. This spectrum exhibits a rhombic $S = 1$ triplet powder pattern at 295 K. The zfs parameters were determined by spectral simulations and yielded $|D/hc| = 0.00578$ cm^{-1} and $|E/hc| = 0.00086$ cm^{-1}. VT EPR spectra for **SQ–Th$_2$–SQ** were also recorded and the doubly-integrated $\Delta m_s = 2$ signal at $g \sim 4$ is shown plotted as a function of inverse temperature (T^{-1}) in Fig. 12B.

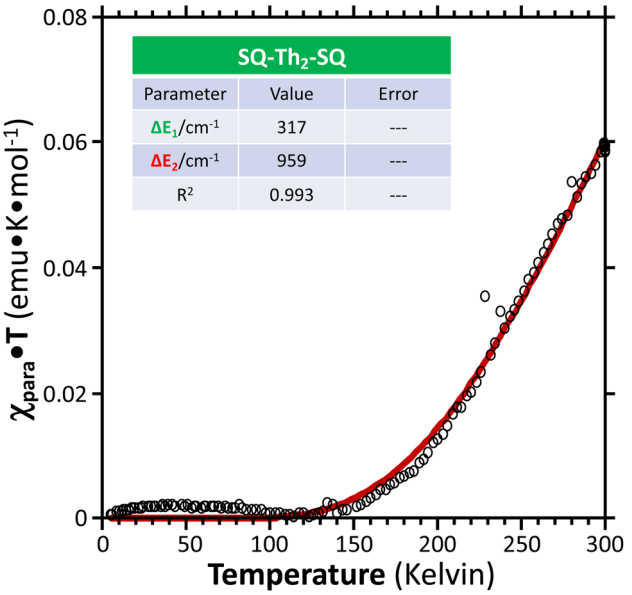

Fig. 11 Paramagnetic susceptibility-temperature product ($\chi_{para}T$) *vs.* temperature (O) for a crystalline sample of **SQ–Th$_2$–SQ**, measured by variable–temperature magnetic susceptibility experiments at a magnetic field strength of 0.1 Tesla. Data were fit (—) to the same model as the VT EPR and EAS data, see Fig. 6B and text. Regarding the magnitude of the $\chi_{para}T$ product in this plot, note that $\chi_{para}T$ is equal to 1.0 emu K mol^{-1} for a pure $S = 1$ triplet state.

Electronic absorption spectroscopy. The VT electronic absorption spectra for **SQ–Th$_2$–SQ** are shown in Fig. 13A and displays panchromatic absorption from the NIR to UV, similar to that of the other complexes in this series. An intense temperature-dependent band is observed at ~12 300 cm^{-1} that, when compared to the VT behavior of **SQ–Th$_3$–SQ**, displays a markedly weaker temperature dependence.

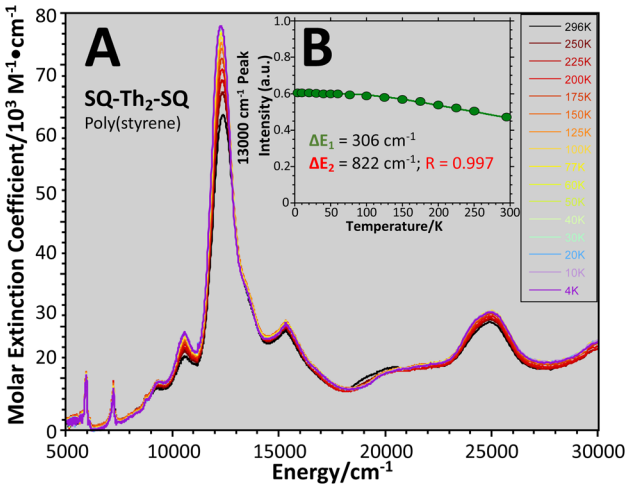

Fig. 13 (A) Variable–temperature (4–298 K) electronic absorption spectra of **SQ–Th$_2$–SQ** in a poly(styrene) film. (B) Normalized transition intensity of 13 000 cm^{-1} band. Data fit using 3 lowest thermally-populated spin states. See Fig. 6B and text.

Analysis of the variable–temperature data. The bond deviation parameters for **SQ–Th$_2$–SQ** indicate a ground state electronic structure description that is between closed-shell quinoidal and open-shell biradical in nature (*i.e.*, a biradicaloid, Fig. 3 and 6B). Here, we analyze the VT magnetic and spectroscopic data to develop insight into the proposed biradicaloid nature of the ground state, and the unusual temperature-dependent behavior of the data. Since the magnetic susceptibility, EPR, and electronic absorption data for **SQ–Th$_2$–SQ** are all temperature dependent, we initially considered the $S = \frac{1}{2}$ dimer model we employed for understanding the temperature dependent data for **SQ–Th$_3$–SQ.** This model incorporates an $S = 0$ singlet ground state and a thermally accessible $S = 1$ triplet state. However, we were unable to obtain a singlet–triplet energy

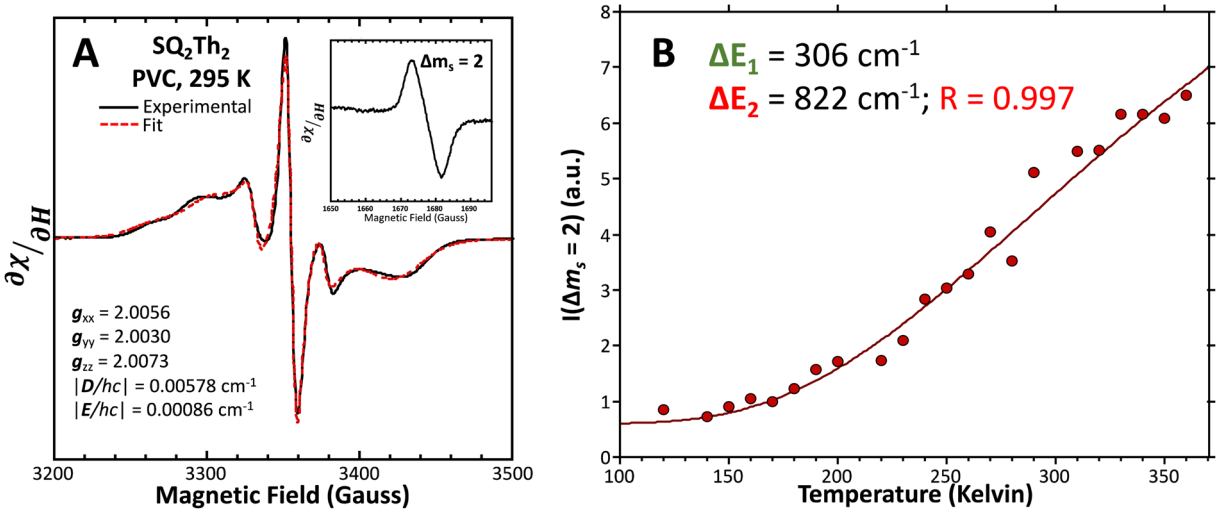

Fig. 12 (A) Powder EPR spectrum of **SQ–Th$_2$–SQ** (—, left). Fit (---) includes 34% $S = \frac{1}{2}$ impurities. For simulation parameters, see text and ESI.† (B) Doubly-integrated $\Delta m_s = 2$ EPR transition intensities (●) *vs.* inverse temperature for **SQ–Th$_2$–SQ**. Samples were ~1 mM dissolved in an evaporated film of poly(vinyl chloride). Data were fit (—) to a model that includes three lowest energy spin states, see text and Fig. 6B.

gap ($2J$) that was consistent with the VT magnetic susceptibility, EPR, and electronic absorption data sets. Therefore, we employed an expanded model (Fig. 6B, gray box) to describe the thermally accessible states in **SQ–Th$_2$–SQ**. This three-state model is comprised of a closed shell ground state ($^1A^{CS}$), with thermally populated open-shell singlet ($^1B_a^{OS}$) and triplet ($^3B_a^{OS}$) exchange-coupled states that are found at energies ΔE_1 and ΔE_2, respectively, above the closed-shell ground state. In this model, the energy difference $\Delta E_1 - \Delta E_2$ corresponds to the singlet–triplet splitting ($2J$) of the open shell biradical states using the exchange Hamiltonian, $\mathscr{H} = -2J\widehat{S_1}\cdot\widehat{S_2}$. Note that these open-shell singlet ($^1B_a^{OS}$) and triplet ($^3B_a^{OS}$) exchange-coupled states were the lowest-lying states in **SQ–Th$_3$–SQ**, and the closed-shell quinoidal state for **SQ–Th$_2$–SQ** represents an electronic excited state in **SQ–Th$_3$–SQ**. We attribute the existence of biradicaloid and aromatic ring-bridged biradical populations to result from a temperature-dependent structural change (increased ring torsion amplitudes, Fig. 14) that leads to greater SQ–Th and Th–Th bond torsions in **SQ–Th$_2$–SQ** as the temperature is increased. Thus, the potential energy surfaces for the open-shell singlet and triplet are described as being distorted along this torsional coordinate, $Q_{torsion}$, relative to the closed shell singlet ground state. Thus, eqn (3) and (4) ($C = N\beta^2/3k_B$ and D represents monoradical impurity), and 5 (C is a proportionality constant) derived from the 3-state model in Fig. 6B were fit to the VT magnetic susceptibility, EPR, and electronic absorption data, respectively.

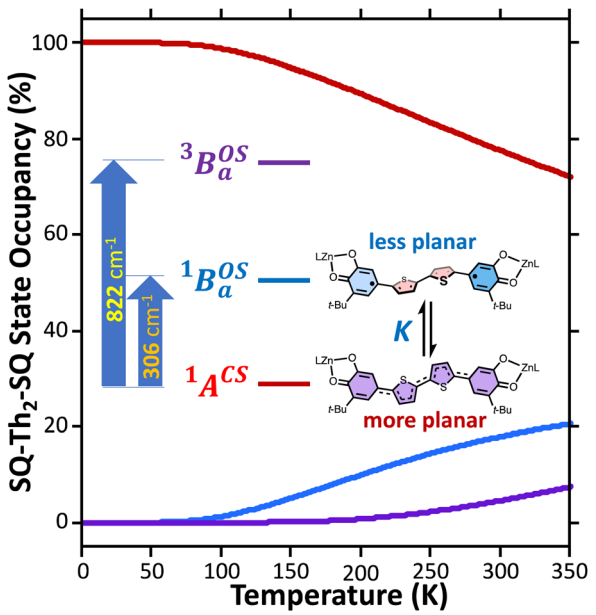

Fig. 14 Equilibrating biradicaloid and aromatic ring-bridged biradical forms that result from a temperature-dependent structural change (*e.g.*, increased ring torsion amplitudes), which leads to greater SQ–Th and Th–Th bond torsions in SQ–Th$_2$–SQ as the temperature is increased. Thus, the potential energy surfaces for the open-shell singlet and triplet are described as being more distorted along this torsional coordinate, $Q_{torsion}$, relative to the closed shell ground state.

$$\chi_{para} = C\frac{g^2}{T}\frac{3e^{\frac{-E_2}{k_BT}}}{1+e^{\frac{-E_1}{k_BT}}+3e^{\frac{-E_2}{k_BT}}} \quad (3)$$

$$I_{EPR} \propto \chi_{para} = C\frac{g^2}{T}\frac{3e^{\frac{-E_2}{k_BT}}}{1+e^{\frac{-E_1}{k_BT}}+3e^{\frac{-E_2}{k_BT}}} + D \quad (4)$$

$$I_{Abs} = C\frac{1}{1+e^{\frac{-E_1}{k_BT}}+3e^{\frac{-E_2}{k_BT}}} \quad (5)$$

Best fits of eqn (3) to the VT magnetic susceptibility data yield $\Delta E_1 = 317\ cm^{-1}$ and $\Delta E_2 = 959\ cm^{-1}$. This results in the open-shell biradical singlet residing only 317 cm^{-1} above the $S = 0$ quinoidal ground state, with a biradical singlet–triplet splitting of $\Delta E_1 - \Delta E_2 = 2J = 642\ cm^{-1}$ ($J = 321\ cm^{-1}$). In contrast to the VT magnetic susceptibility data, the VT EPR data directly probes the thermally populated open-shell triplet state as a spectroscopic observable. The best fit of eqn (4) to the VT EPR data gives $\Delta E_1 = 306\ cm^{-1}$ and $\Delta E_2 = 822\ cm^{-1}$. The $\Delta E_1 = 306\ cm^{-1}$ quinoid – biradical singlet–singlet gap is in remarkable agreement with that determined from the VT magnetic susceptibility experiments ($\Delta E_1 = 317\ cm^{-1}$). However, the $\Delta E_1 - \Delta E_2 = 2J = 516\ cm^{-1}$ ($J = 258\ cm^{-1}$) determined for the biradical singlet–triplet gap in the solid solution (polymer) phase is reduced by ~20% compared to that determined by magnetic susceptibility experiments on samples in the polycrystalline state.

Eqn (5) was fit to the VT electronic absorption data, which directly probes the reduction in closed-shell biradicaloid singlet state population with increasing temperature by monitoring the temperature dependence of the ~12 300 cm^{-1} absorption band. The VT absorption data were collected in the solid solution (polymer matrix) phase and the temperature dependence is described with the same ΔE_1 and ΔE_2 parameters that were determined from the temperature dependence of the $\Delta m_s = 2$ EPR resonance. Thus, VT magnetic susceptibility, EPR, and electronic absorption spectroscopy all yield the same energy gap for populating the biradical singlet state ($\Delta E_{1\ ave} = 310\ cm^{-1}$). The experimentally determined Boltzmann populations of the three thermally-accessible states for **SQ–Th$_2$–SQ** are presented graphically in Fig. 14. The biradical character present in the $^1A^{CS}$ ground state must therefore derive from strong configurational mixing with open shell singlet biradical excited state(s), and this is described in the state energy diagram depicted in Fig. 6B (*e.g.*, $^1A^{CS}$ mixing with $^1A^{OS}$).

In order to address whether the thermally-excited $^1B_a^{OS}$ state of **SQ–Th$_2$–SQ** possesses any appreciable closed-shell singlet character, or whether this state is analogous to the aromatic biradical singlet ground state of **SQ–Th$_3$–SQ**, we analyzed the distance dependence of the $^1B_a^{OS} - {}^3B_a^{OS}$ singlet–triplet splitting in **SQ–Th$_2$–SQ** and **SQ–Th$_3$–SQ**. We have previously determined the distance decay constant ($\beta = 0.22$) for magnetic exchange mediated by aromatic thiophene bridges.[21] Since β should be a transferrable property[74,75] for evaluating magnetic exchange mediated by these thiophene units, we have used this β value

and the $J_{SQ-SQ}(ave) = -279\ cm^{-1}$ for **SQ–Th$_2$–SQ**, which was the average derived from magnetic susceptibility, VT EPR, and VT electronic absorption spectroscopy, to derive the expected J value for **SQ–Th$_3$–SQ**. This analysis predicts $J \approx -119\ cm^{-1}$ for **SQ–Th$_3$–SQ**, which is in excellent agreement with the experimental $J_{ave} = -117\ cm^{-1}$ that we determined for **SQ–Th$_3$–SQ**. This analysis provides strong support for the $\Delta E_1 - \Delta E_2$ gap representing the $J_{SQ\text{-}SQ}$Heisenberg exchange interaction in both **SQ–Th$_2$–SQ** and **SQ–Th$_3$–SQ**, with an openshell biradical ground state configuration for **SQ–Th$_3$–SQ**, and thermally accessible open-shell triplet biradical states for both **SQ–Th$_2$–SQ** and **SQ–Th$_3$–SQ**.

Discussion

Biradicals are distinguished by the presence of singlet and triplet configurations that derive from a HOMO → LUMO one-electron promotion relative to the closed-shell quinoidal ground state. These configurations are described by the quinoid and biradical Lewis structures presented in Fig. 1. For biradicaloids, the ground state open-shell biradical character has been described in terms of a biradical index (y_i), which may be computed from natural orbital occupancies that derive from the results of spin unrestricted Hartree–Fock or DFT computations.[1] Here, y_0 derives from the occupancy of the lowest unoccupied natural orbital, and is often used to describe the degree of biradical character in the electronic ground state.[1] Additionally, a valence configuration interaction model, effectively related to the 4-state Anderson model[68] that has had a tremendous influence on our understanding of antiferromagnetic exchange in dimeric systems, has been employed to evaluate the degree of biradical character.[1,69] This model derives from the asymptotic limit of the H_2 molecule (very weak radical–radical coupling with no bridge orbitals) involving two effectively degenerate orbitals and the incorporation of closed-shell ionic configurations. This 2-electron, 2-orbital (4-state) model allows for configurational mixing between closed and open shell singlet configurations with ionic and covalent character. If coupling between the SQ SOMO orbitals (also a 2-electron, 2-orbital model) in actual or effective symmetry is assumed *a priori*, configurational mixing between closed- and open-shell singlets is symmetry forbidden. Since there are notable examples where an expanded model is required to explain the electronic structure and the nature of the radical–radical exchange interaction in biradical systems,[21,57–61,76–80] we have minimally expanded the 2-electron, 2-orbital model to include a doubly-occupied bridge orbital that provides a mechanism for understanding the nature of open-shell singlet states that configurationally mix with quinoidal states.[21,57–61,67,77,78]

With respect to the role of the thiophene bridge units in defining the ground state electronic and geometric structure of the **SQ–Th$_n$–SQ** series, the explicit consideration and addition of a single bridge-orbital reveals how open-shell and low-energy closed-shell singlet configurations (*e.g.*, $^1A^{OS}$ and $^1A^{CS}$, respectively; Fig. 5B and 6) can mix to yield "biradicaloid" electronic structures in both ground- (Fig. 6B) and excited (Fig. 6C) states. We note that the nature of these open-shell singlet states generally need not be formal biradical states (analogous to $^1B_a^{OS}$ in the 3-orbital model) but could be any open-shell configuration of the proper symmetry to allow for configurational mixing with closed shell-singlet configurations (see Fig. 5 and 6 – *e.g.* $^1A^{OS}$ Fig. 5b). As a consequence, the cases presented here show how open-shell/closed-shell $^1A^{OS}$–$^1A^{CS}$ mixing contributes to modifying the degree of quinoidal-aromatic bond patterns in the thiophene bridge fragments. Although this configurational mixing leads to complex ground- and excited state electronic structures in these systems, a key experimental descriptor of the degree of biradical character in the electronic ground states is given by the experimentally derived bond deviation parameters $\Sigma|\Delta_i|$,[62] which can then be correlated with experimental magnetic and spectroscopic observables. This allows results of electronic structure computations to be evaluated in the context of the experimental data.

Regarding the concepts of quinoidal, biradical, and biradicaloid electronic structure descriptions, one needs to consider how these are defined. For example, the quinoidal closed-shell singlet configuration can mix with other closed- or open-shell singlet configurations of the same symmetry. One of these open-shell configurations is associated with what is described as possessing "biradical" character, where the unpaired electrons are primarily localized on the "radical" moieties of the molecule. Thus, from a Lewis structure approach, we define a true biradicaloid as representing a resonance hybrid comprised of the quinoidal and biradical Lewis structures depicted in Fig. 1. Typically, non-contributing or marginally contributing resonance structures describing the ground state (*i.e.*, the biradical forms of **SQ–SQ** and **SQ–Th–SQ**) are thought of as representing high energy configurations. However, this is not necessarily correct. The dioxolene-bridge-dioxolene fragments of **SQ–SQ** and **SQ–Th$_2$–SQ** possess C_{2h} symmetry, and the closed-shell quinoid configuration and open-shell biradical configuration are forbidden to mix by symmetry even though they may be very close in energy. This is clearly highlighted for **SQ–Th$_2$–SQ**, where the quinoid and biradical singlet configurations are within k_BT of one another but possess different symmetries and do not mix. For these molecules, the biradicaloid character admixed into the ground-state configuration is best described as open-shell singlet character, since there is no resonance between the two Lewis structures drawn in Fig. 1. We therefore describe a ground-state electronic structure description of **SQ–Th$_2$–SQ** as being quinoidal, with open-shell singlet character.

The low-energy thermally populated excited states are biradical in nature and possess **SQ–SQ** radical–radical Heisenberg exchange coupling interactions. The thermally accessible biradical states in **SQ–Th$_2$–SQ** and **SQ–Th$_3$–SQ** possess experimentally determined J values that are consistent with previously determined distance decay parameters (β values) for aromatic SQ bridge configurations.[21] These low-energy open-shell states possess non-planar geometries. We suggest that this symmetry lowering derives from a two-stage pseudo Jahn–Teller effect,[81] which involves vibronic coupling with specific excited states to electronically drive out-of-plane ring–ring distortions.

The **SQ–Th$_n$–SQ** (n = 0–3) molecules presented in this study provide clear examples of dominantly closed-shell quinoidal (**SQ–Th$_n$–SQ**; n = 0, 1) and open-shell biradical (**SQ–Th$_3$–SQ**) ground states. The **SQ–Th$_2$–SQ** complex is unique in this series, possessing some open-shell singlet character as evidenced by the experimentally-determined bridge bond deviation values ($\Sigma|\Delta_i|$).[62] Although the open shell biradical state of **SQ–Th$_2$–SQ** is a mere 310 cm^{-1} above the quinoidal ground state, these states do not configurationally mix due to symmetry constraints. This thermally excited biradical state in **SQ–Th$_2$–SQ** becomes the ground state in **SQ–Th$_3$–SQ** (see Fig. 6). Additional evidence for admixed open- and closed-shell character in the ground state of **SQ–Th$_2$–SQ** is found in the excited states of **SQ–Th$_3$–SQ**, as revealed by the dramatic differences in spin-allowed ^{1}GS → ^{1}ES (ES = excited state configuration) and ^{3}GS → ^{3}ES transitions (*e.g.* the $^1B_a^{OS} \rightarrow {}^1$ES and $^3B_a^{OS} \rightarrow {}^3$ES transitions in Fig. 10). This mixing of open- and closed-shell excited states naturally derives from our 3-orbital, 4-electron model that indicates the importance of bridge states in the description of closed-shell quinoidal, open-shell biradical, and admixed singlet biradical character in the ground and excited states of these molecules. Our study reveals of the power of using a combined synthetic, spectroscopic, and magnetic approach to unravel the complex nature of these and related molecules.

Conclusions

In summary, the degree of closed shell quinoidal and open-shell aromatic character in the electronic ground state and thermally accessible excited states of **SQ–Th–SQ**, **SQ–Th$_2$–SQ**, and **SQ–Th$_3$–SQ** are markedly different. The expanded 3-orbital model discussed in this work has provided insight into the nature of the closed-shell ground state singlet in **SQ–Th–SQ**, an open-shell singlet for **SQ–Th$_3$–SQ**, and a configurationally mixed singlet ground state for **SQ–Th$_2$–SQ**, which possesses some open-shell character. The pattern of bridge bond lengths shown in Fig. 3 is consistent with the predictions enabled by this model, and reveals the alternation of short- and long C–C bonds characteristic of quinoidal resonance structures being most prominent for **SQ–Th–SQ** and least prominent for **SQ–Th$_3$–SQ**. In addition, the dioxolene bond deviation parameters[62] ($\Sigma|\Delta_i|$) clearly decrease from **SQ–Th–SQ** to **SQ–Th$_3$–SQ**, and this indicates maximal quinoidal character for **SQ–Th–SQ**. The results of our structural analyses are consistent with EPR, electronic absorption spectroscopy, and magnetic susceptibility studies for all of these complexes.

A primary strength of our approach to the biradicaloid problem lies in the simplicity of using symmetry/group theory to understand state mixing, and this is further exemplified by our use of a conceptually approachable, minimal basis 4-electron-, 3-orbital model that includes the bridge moiety. Thus, the degree of open-shell, closed-shell, and biradical character in the electronic ground state is determined by the molecular symmetry, and is modulated by the nature and of the bridge fragment (*e.g.*, thiophene, phenylene, *etc.* and the number of bridge units). Doubly-excited states (*e.g.*, $^1A^{DECS}$; Fig. 5B) and open-shell singlet states with occupied π* and/or vacant π-bonding orbitals can attenuate the quinoidal bond length alternation pattern for closed-shell states if they have the same symmetry as the ground state. However, open-shell (*e.g.*, $^{1,3}B_a^{OS}$) states have non-quinoidal, aromatic bridge units and do not mix with closed-shell singlet states. Importantly, the dioxolene moieties provide attenuated spin density in this series of compounds that allows for exemplars of quinoid, configurationally mixed quinoid/open-shell, and open-shell singlet biradical ground states in the complexes that we have detailed here. We are not aware of any other series of molecules that highlight the complex electronic structures associated with open-shell/closed-shell mixing as a function of the bridge repeat unit. Ongoing studies are focusing on spectral band assignments, correlating open-shell character with bond deviation parameters,[62] and understanding how different bridges and metal ions can fine tune the nature of open- and closed-shell configurational mixing in analogs of the **SQ–Th$_n$–SQ** series.

Data availability

ESI† contains synthetic- and characterization details of all new molecules and metal complexes.

Author contributions

M. L. K. and D. A. S. conceptualized and supervised the project; P. D. M. synthesized and characterized all molecules and complexes; J. M. collected and analyzed variable temperature electronic absorption spectra; P. D. M., D. A. S., and M. L. K. wrote the original manuscript draft.

Conflicts of interest

The authors declare no competing financial interests.

Acknowledgements

D. A. Shultz thanks the National Science Foundation (CHE-1931291 and CHE-1764181) for financial support. M. L. Kirk acknowledges the National Science Foundation (NSF CHE-1900237) for financial support.

References

1 T. Y. Gopalakrishna, W. Zeng, X. Lu and J. Wu, *Chem. Commun.*, 2018, **54**, 2186–2199.
2 J. J. Dressler, M. Teraoka, G. L. Espejo, R. Kishi, S. Takamuku, C. J. Gomez-Garcia, L. N. Zakharov, M. Nakano, J. Casado and M. M. Haley, *Nat. Chem.*, 2018, **10**, 1134–1140.
3 Y. Shen, G. Xue, Y. Dai, S. M. Quintero, H. Chen, D. Wang, F. Miao, F. Negri, Y. Zheng and J. Casado, *Nat. Commun.*, 2021, **12**, 6262.
4 R. Rausch, M. I. S. Rohr, D. Schmidt, I. Krummenacher, H. Braunschweig and F. Wurthner, *Chem. Sci.*, 2021, **12**, 793–802.
5 M. Abe, *Chem. Rev.*, 2013, **113**, 7011–7088.

6 A. Hinz, J. Bresien, F. Breher and A. Schulz, *Chem. Rev.*, 2023, **123**, 10468–10526.
7 C. K. Frederickson, B. D. Rose and M. M. Haley, *Acc. Chem. Res.*, 2017, **50**, 977–987.
8 F. A. Larik, M. Faisal, A. Saeed, Q. Abbas, M. A. Kazi, N. Abbas, A. A. Thebo, D. M. Khan and P. A. Channar, *J. Mater. Sci.: Mater. Electron.*, 2018, **29**, 17975–18010.
9 Y. Dai, Z. Xie, M. Bao, C. Liu and Y. H. Su, *Chem. Sci.*, 2023, **14**, 3548–3553.
10 L. Li, J. Z. Low, J. Wilhelm, G. Liao, S. Gunasekaran, C. R. Prindle, R. h. L. Starr, D. Golze, C. Nuckolls, M. L. Steigerwald, F. Evers, L. M. Campos, X. Yin and L. Venkataraman, *Nat. Chem.*, 2022, **14**, 1061–1067.
11 I. Bergenti, V. Dediu, M. Prezioso and A. Riminucci, *Philos. Trans. R. Soc., A*, 2011, **369**, 3054–3068.
12 A. Konishi, Y. Hirao, H. Kurata, T. Kubo, M. Nakano and K. Kamada, *Pure Appl. Chem.*, 2014, **86**, 497–505.
13 M. L. Kirk, D. A. Shultz, P. Hewitt and A. van der Est, *J. Am. Chem. Soc.*, 2022, **144**, 12781–12788.
14 M. L. Kirk, D. A. Shultz, P. Hewitt and A. van der Est, *J. Phys. Chem. Lett.*, 2022, **13**, 872–878.
15 M. L. Kirk, D. A. Shultz, P. Hewitt, D. E. Stasiw, J. Chen and A. van der Est, *Chem. Sci.*, 2021, **12**, 13704–13710.
16 M. L. Kirk, D. A. Shultz, J. Chen, P. Hewitt, D. Daley, S. Paudel and A. van Der Est, *J. Am. Chem. Soc.*, 2021, **143**, 10519–10523.
17 M. L. Kirk, D. A. Shultz, A. R. Marri, P. Hewitt and A. van der Est, *J. Am. Chem. Soc.*, 2022, **144**, 21005–21009.
18 H. Sato, V. Kathirvelu, G. Spagnol, S. Rajca, A. Rajca, S. S. Eaton and G. R. Eaton, *J. Phys. Chem. B*, 2008, **112**, 2818–2828.
19 S. Gunasekaran, D. Hernangómez-Pérez, I. Davydenko, S. Marder, F. Evers and L. Venkataraman, *Nano Lett.*, 2018, **18**, 6387–6391.
20 L. Li, S. G. Louie, A. M. Evans, E. Meirzadeh, C. Nuckolls and L. Venkataraman, *J. Am. Chem. Soc.*, 2023, **145**, 2492–2498.
21 M. L. Kirk, D. A. Shultz, D. E. Stasiw, G. F. Lewis, G. Wang, C. L. Brannen, R. D. Sommer and P. D. Boyle, *J. Am. Chem. Soc.*, 2013, **135**, 17144–17154.
22 G. C. Solomon, D. Q. Andrews, T. Hansen, R. H. Goldsmith, M. R. Wasielewski, R. P. Van Duyne and M. A. Ratner, *J. Chem. Phys.*, 2008, **129**, 054701.
23 W. B. Davis, W. A. Svec, M. A. Ratner and M. R. Wasielewski, *Nature*, 1998, **396**, 60–63.
24 P. F. Barbara, T. J. Meyer and M. A. Ratner, *J. Phys. Chem.*, 1996, **100**, 13148–13168.
25 W. P. Su, J. R. Schrieffer and A. J. Heeger, *Phys. Rev. Lett.*, 1979, **42**, 1698–1701.
26 A. J. Heeger, S. Kivelson, J. R. Schrieffer and W. P. Su, *Rev. Mod. Phys.*, 1988, **60**, 781–850.
27 Z. Zeng, Y. M. Sung, N. Bao, D. Tan, R. Lee, J. L. Zafra, B. Y. Lee, M. Ishida, J. Ding, J. T. Lopez Navarrete, Y. Li, W. Zeng, D. Kim, K.-W. Huang, R. D. Webster, J. Casado and J. Wu, *J. Am. Chem. Soc.*, 2012, **134**, 14513–14525.
28 J. Wang, X. Xu, H. Phan, T. S. Herng, T. Y. Gopalakrishna, G. Li, J. Ding and J. Wu, *Angew. Chem., Int. Ed.*, 2017, **56**, 14154–14158.
29 P. Ravat and M. Baumgarten, *PCCP Phys. Chem. Chem. Phys.*, 2015, **17**, 983–991.
30 T. Takahashi, K. I. Matsuoka, K. Takimiya, T. Otsubo and Y. Aso, *J. Am. Chem. Soc.*, 2005, **127**, 8928–8929.
31 D. Sakamaki, S. Yano, T. Kobashi, S. Seki, T. Kurahashi, S. Matsubara, A. Ito and K. Tanaka, *Angew. Chem., Int. Ed.*, 2015, **54**, 8267–8270.
32 S. Di Motta, F. Negri, D. Fazzi, C. Castiglioni and E. V. Canesi, *J. Phys. Chem. Lett.*, 2010, **1**, 3334–3339.
33 K. Takahashi, A. Gunji, K. Yanagi and M. Miki, *J. Org. Chem.*, 1996, **61**, 4784–4792.
34 F. Tampieri, L. Colella, A. Maghsoumi, J. Martí-Rujas, E. Parisini, M. Tommasini, C. Bertarelli and A. Barbon, *J. Phys. Chem. C*, 2016, **120**, 5732–5740.
35 M. Lanata, C. Bertarelli, M. C. Gallazzi, A. Bianco, M. Del Zoppo and G. Zerbi, *Synth. Met.*, 2003, **138**, 357–362.
36 R. West, J. A. Jorgenson, K. L. Stearley and J. C. Calabrese, *Chem. Commun.*, 1991, 1234–1235, DOI: **10.1039/C39910001234**.
37 J. Pannell, *Chem. Ind.*, 1962, 1797–1800.
38 K. Takahashi, T. Suzuki, K. Akiyama, Y. Ikegami and Y. Fukazawa, *J. Am. Chem. Soc.*, 1991, **113**, 4576–4583.
39 K. Takahashi, A. Gunji, K. Yanagi and M. Miki, *J. Org. Chem.*, 1996, **61**, 4784–4792.
40 K. Takahashi and T. Suzuki, *J. Am. Chem. Soc.*, 1989, **111**, 5483–5485.
41 j. Rebmann, J. Zhou, P. Schuler, H. B. Stegmann and A. Rieker, *J. Chem. Res., Synop.*, 1996, **7**, 318–319.
42 A. Rebmann, J. Zhou, P. Schuler, A. Rieker and H. B. Stegmann, *J. Chem. Soc., Perkin Trans. 2*, 1997, **2**, 1615–1618.
43 A. E. Chichibabin, *Ber. Dtsch. Chem. Ges.*, 1907, **40**, 1810–1819.
44 H. M. McConnell, *J. Chem. Phys.*, 1960, **33**, 1868–1869.
45 Y. Kanzaki, D. Shiomi, K. Sato and T. Takui, *J. Phys. Chem. B*, 2012, **116**, 1053–1059.
46 T. Kubo, *Chem. Lett.*, 2015, **44**, 111–122.
47 E. Müller and I. Müller-Rodloff, *Adv. Cycloaddit.*, 1935, **517**, 134–151.
48 H. S. Jarrett, G. J. Sloan and W. R. Vaughan, *J. Chem. Phys.*, 1956, **25**, 697–701.
49 D. C. Reitz and S. I. Weissman, *J. Chem. Phys.*, 1960, **33**, 700–704.
50 L. K. Montgomery, J. C. Huffman, E. A. Jurczak and M. P. Grendze, *J. Am. Chem. Soc.*, 1986, **108**, 6004–6011.
51 R. K. Waring and G. J. Sloan, *J. Chem. Phys.*, 1964, **40**, 772–777.
52 H.-D. Brauer, H. tieger, J. S. Hyde, L. D. Kispert and G. R. Luckhurst, *Mol. Phys.*, 1969, **17**, 457–471.
53 M. Ruf, K. Weis and H. Vahrenkamp, *J. Chem. Soc., Chem. Commun.*, 1994, 135–136.
54 M. Ruf and H. Vahrenkamp, *Inorg. Chem.*, 1996, **35**, 6571–6578.
55 M. Ruf, B. C. Noll, M. D. Groner, G. T. Yee and C. G. Pierpont, *Inorg. Chem.*, 1997, **36**, 4860–4865.
56 J. Chen, J. Yang, M. Yadav, D. A. Shultz and M. L. Kirk, *Inorg. Chem.*, 2023, **62**, 739–747.

57 D. A. Shultz, M. L. Kirk, J. Zhang, D. E. Stasiw, G. Wang, J. Yang, D. Habel-Rodriguez, B. W. Stein and R. D. Sommer, *J. Am. Chem. Soc.*, 2020, **142**, 4916–4924.
58 M. L. Kirk and D. A. Shultz, *Coord. Chem. Rev.*, 2013, **257**, 218–233.
59 M. L. Kirk, D. A. Shultz, E. C. Depperman, D. Habel-Rodriguez and R. D. Schmidt, *J. Am. Chem. Soc.*, 2012, **134**, 7812–7819.
60 M. L. Kirk, D. A. Shultz, D. Habel-Rodriguez, R. D. Schmidt and U. Sullivan, *J. Phys. Chem. B*, 2010, **114**, 14712–14716.
61 M. L. Kirk, D. A. Shultz, E. C. Depperman and C. L. Brannen, *J. Am. Chem. Soc.*, 2007, **129**, 1937–1943.
62 S. H. Bodnar, A. Caneschi, A. Dei, D. A. Shultz and L. Sorace, *Chem. Commun.*, 2001, 2150–2151.
63 P. Pouzet, I. Erdelmeier, D. Ginderow, P. M. Dansette, D. Mansuy and J.-P. Mornon, *J. Heterocycl. Chem.*, 1997, **34**, 1567–1574.
64 R. Akai, K. Oka, R. Nishida and N. Tohnai, *CrystEngComm*, 2022, **24**, 4180–4186.
65 D. D. Graf, R. G. Duan, J. P. Campbell, L. L. Miller and K. R. Mann, *J. Am. Chem. Soc.*, 1997, **119**, 5888–5899.
66 O. Kahn, *Molecular Magnetism*, VCH, New York, 1993.
67 M. L. Kirk, D. A. Shultz and E. C. Depperman, *Polyhedron*, 2005, **24**, 2880–2884.
68 P. W. Anderson, *Phys. Rev.*, 1959, **115**, 2–13.
69 J. Michl and V. Bonacic-Koutecky, *Electronic Aspects of Organic Photochemistry*, Wiley-Interscience, New York, 1990.
70 R. Nieman, N. J. Silva, A. J. A. Aquino, M. M. Haley and H. Lischka, *J. Org. Chem.*, 2020, **85**, 3664–3675.
71 Y. Tanabe and S. Sugano, *J. Phys. Soc. Jpn.*, 1954, **9**, 753–766.
72 S. Sugano, Y. Tanabe and H. Kamimura, *Multiplets of Transition-Metal Ions in Crystals*, Academic Press, New York, 1970.
73 E. Wasserman, L. C. Snyder and W. A. Yager, *J. Chem. Phys.*, 1964, **41**, 1763–1772.
74 C. Herrmann, *J. Phys. Chem. A*, 2019, **123**, 10205–10223.
75 M. L. Kirk, R. Dangi, D. Habel-Rodriguez, J. Yang, D. A. Shultz and J. Zhang, *Chem. Sci.*, 2020, **11**, 11425–11434.
76 P. Hewitt, D. A. Shultz and M. L. Kirk, *J. Org. Chem.*, 2021, **86**, 15577–15587.
77 D. E. Stasiw, J. Zhang, G. Wang, R. Dangi, B. W. Stein, D. A. Shultz, M. L. Kirk, L. Wojtas and R. D. Sommer, *J. Am. Chem. Soc.*, 2015, **137**, 9222–9225.
78 M. L. Kirk, D. A. Shultz, D. E. Stasiw, D. Habel-Rodriguez, B. Stein and P. D. Boyle, *J. Am. Chem. Soc.*, 2013, **135**, 14713–14725.
79 M. L. Kirk, D. A. Shultz, R. D. Schmidt, D. Habel-Rodriguez, H. Lee and J. Lee, *J. Am. Chem. Soc.*, 2009, **131**, 18304–18313.
80 F. Miao, Y. R. Ji, B. Han, S. M. Quintero, H. Chen, G. Xue, L. Cai, J. Casado and Y. Zheng, *Chem. Sci.*, 2023, **14**, 2698–2705.
81 A. Toyota, S. Koseki and M. Shiota, *J. Phys. Chem. A*, 2000, **104**, 5343–5350.